nature nanotechnology

Article

https://doi.org/10.1038/s41565-022-01283-1

Multi-micron crisscross structures grown from DNA-origami slats

Received: 25 April 2022

Accepted: 27 October 2022

Published online: 21 December 2022

Check for updates

Christopher M. Wintersinger[1,2,3,4,9], Dionis Minev[1,2,3,4,9], Anastasia Ershova[1,3,4,9], Hiroshi M. Sasaki[1,5,7], Gokul Gowri[1,3,4,5], Jonathan F. Berengut[1,3,6], F. Eduardo Corea-Dilbert[3,8], Peng Yin[1,5] & William M. Shih[1,3,4]

Living systems achieve robust self-assembly across a wide range of length scales. In the synthetic realm, nanofabrication strategies such as DNA origami have enabled robust self-assembly of submicron-scale shapes from a multitude of single-stranded components. To achieve greater complexity, subsequent hierarchical joining of origami can be pursued. However, erroneous and missing linkages restrict the number of unique origami that can be practically combined into a single design. Here we extend crisscross polymerization, a strategy previously demonstrated with single-stranded components, to DNA-origami 'slats' for fabrication of custom multi-micron shapes with user-defined nanoscale surface patterning. Using a library of ~2,000 strands that are combinatorially arranged to create unique DNA-origami slats, we realize finite structures composed of >1,000 uniquely addressable slats, with a mass exceeding 5 GDa, lateral dimensions of roughly 2 μm and a multitude of periodic structures. Robust production of target crisscross structures is enabled through strict control over initiation, rapid growth and minimal premature termination, and highly orthogonal binding specificities. Thus crisscross growth provides a route for prototyping and scalable production of structures integrating thousands of unique components (that is, origami slats) that each is sophisticated and molecularly precise.

In structural DNA nanotechnology[1–27], the scaffolded DNA-origami method affords robust self-assembly of arbitrary two- and three-dimensional nanoscale objects[1–6]. The oligonucleotide 'staple' strands are designed to lack complementarity to each other, and folding is exactly controlled by a long single-stranded DNA (ssDNA) scaffold that is substoichiometric with respect to the staple strands, resulting in one-to-one conversion of scaffold particles into origami. This absolute scaffold dependence enables assembly over a broad range of temperatures and salt concentrations, while circumventing accumulation of incomplete assemblies or by-products. Due to their robust folding performance, origami offers a user-friendly approach for creating structures with addressable features. Applications have included plasmonic devices relying on placement of nanoparticles[28,29], therapeutic devices with spatial control over cargos that sense the

[1] Wyss Institute for Biologically Inspired Engineering, Harvard University, Boston, MA, USA. [2] John A. Paulson School of Engineering and Applied Sciences, Harvard University, Boston, MA, USA. [3] Department of Cancer Biology, Dana-Farber Cancer Institute, Boston, MA, USA. [4] Department of Biological Chemistry and Molecular Pharmacology, Harvard Medical School, Boston, MA, USA. [5] Department of Systems Biology, Harvard Medical School, Boston, MA, USA. [6] EMBL Australia Node for Single Molecule Science, School of Medical Sciences, The University of New South Wales, Sydney, NSW, Australia. [7] Present address: 10x Genomics, Inc., Pleasanton, CA, USA. [8] Present address: Geisel School of Medicine at Dartmouth, Hanover, NH, USA. [9] These authors contributed equally: Christopher M. Wintersinger, Dionis Minev, Anastasia Ershova. e-mail: William_Shih@dfci.harvard.edu

in vivo environment[30,31] and research tools that place biomolecules in specified arrangements to deduce their biophysical properties[32,33].

One limitation of DNA origami is that their maximal size is limited to ~5 MDa because the shape is bounded by the length of the scaffold DNA. While it is possible to use longer scaffold sequences, they are difficult to obtain in ssDNA form and are delicate to handle because they are prone to shearing[7–9]. DNA bricks[10–13] may instead be used to create structures many times larger than a single origami, with as many as 30,000 unique monomers and a total mass of ~0.5 GDa per assembled particle. In contrast to origami 'staple' strands, DNA tiles and bricks are complementary to each other, thus eliminating the scaffold dependence of the assembly. However, spontaneous association of building blocks effectively limits the yield for such single-pot growth processes and increases the burden for post-assembly purification[26]. Additionally, for the largest of such structures, current pricing on nanomole-scale oligonucleotide synthesis can be cost-prohibitive. For example, assembly of a 0.5 GDa megastructure required ~30,000 distinct 52mers, at a cost of roughly US$150,000, with a final yield of ~1%.

Hierarchical approaches can be used, but achieving assemblies containing more than a few distinct DNA nanostructures has been challenging[14–24] (see Supplementary Text 1 for discussion of hierarchical and periodic DNA-origami assembly methods). In the most complex demonstration in terms of the number of unique DNA origamis to date, structures consisting of 64 unique DNA-origami components were constructed using a method termed fractal assembly. To suppress off-target joining of DNA-origami monomers, three sequential steps were employed to build 4-component, then 16-component and finally 64-component supershapes[25]. Fine-tuning of monomer stoichiometries and reaction temperatures were required, nevertheless reported yields dropped from ~93% to ~48% to ~2% for the three steps, respectively. Despite only four subassemblies coming together per stage and precise care in preparation, unfinished, erroneous and aggregated by-products led to rapidly diminishing yields as more unique monomers and assembly stages were added. Thus fractal assembly in this way appears effective for hierarchical constructions with dozens of components, but may face severe yield issues when larger numbers of parts are desired.

Previously we introduced crisscross polymerization of ssDNA slats for robust control over nucleation[26]; here, we generalize this method to operate with DNA-origami slats—which are over two orders of magnitude larger than their ssDNA counterparts—for synchronous initiation of growth of target supershapes from relatively small seeds. Using 6-helix bundle (6HB)[22,34,35] and 12-helix bundle (12HB) nanorods extending weak binding handles along their lengths, we created a diversity of finite and periodic assemblies. The number of fully formed assemblies is controlled exactly by the amount of seed added, with the robustness of growth from hundreds of origami-based parts comparable to that of origami folding itself from similar numbers of much smaller components.

Design of the DNA-origami slats

In crisscross polymerization, an incoming slat must engage with a large number of other slats (up to either 8 or 16 in this study) for stable attachment to the edge of a growing structure; this requirement for a high level of coordination is the basis for the robustness of crisscross against unwanted spurious nucleation[26] (Supplementary Fig. 1). To meet this design criterion, each individual pairwise interaction must be quite weak at the desired temperature of growth and ideally far below this temperature as well. For ssDNA slats, this was achieved with interactions that span just a half turn of DNA (that is, 5 or 6 bp)[26]. We hypothesized that crisscross assembly could also be implemented for DNA-origami slats by engineering sufficiently weak binding handles. Then to bypass the nucleation barrier in a controlled fashion, preformed seeds could be employed that use much stronger binding interactions to capture an initial set of 'nucleating' slats in an arrangement that resembles a critical nucleus (Supplementary Fig. 1b(i),(ii)). Consequently, a cascade of energetically favourable downstream assembly steps could propagate growth (Fig. 1a and Supplementary Fig. 1b(iii)–(v)).

As a convenient shorthand, we refer to any designed DNA-based assembly that consists of roughly a million or more nucleotides as 'megastructures'. To achieve crisscross growth of megastructures from DNA-origami building blocks, we designed 6HB and 12HB slats that assemble by nucleating upon a gridiron-origami[6] seed (Fig. 1a and Supplementary Fig. 2a). The 3′ ends of staple strands on the top and bottom helices of each slat were encoded with ssDNA binding handles to link the slats to one another, although each could alternatively be programmed as an addressable 'node' that engages a desired cargo (Fig. 1b(i) and Supplementary Fig. 2b(i),(ii)). The 6HB is ~450 nm long and features 32 handle positions spaced ~14 nm apart along its length; the 12HB is ~225 nm long with 16 positions along its length (see Supplementary Text 2 and Supplementary Fig. 3 for more discussion of the 12HB design). As depicted in red in Fig. 1a and in Supplementary Fig. 2a(iii), the seed has 16 columns of five 'sockets', where each column captures an individual 'nucleating' slat with five 10 nucleotide (nt) handles that each 'plug' into its complementary socket (Supplementary Fig. 2b(iii) and Fig. 1b(ii)). We validated folding of 6HB slats, 12HB slats and seeds by imaging with negative-stain transmission electron microscopy (TEM) (Supplementary Figs. 4 and 5).

We tested unseeded formation of sample crisscross structures with 10, 9, 8, 7 or 6 nt handles to explore how handle length affects spurious nucleation as a function of temperature. The 10, 9 and 8 nt handles were found to yield significant unseeded assembly at relevant temperatures (Supplementary Fig. 6a–c(i)). However, this was not observed with either the 7 or 6 nt handles (Supplementary Fig. 6c(ii),(iii)). Hence, we narrowed our focus to 7 nt handles, affording greater thermal stability versus 6 nt handles, for creating origami-slat megastructures (Fig. 1c,d). The algorithm for designing the sequence handles, computed energies versus handle length, and need for poly-T linkers are described in Supplementary Text 3, and Supplementary Figs. 7 and 8, respectively.

Finite megastructures

We conceived of many finite and periodic megastructures that could be made from two perpendicular layers of the DNA slats (Fig. 1c,d). We selected 32 isoenergetic 7 nt handle sequences and purchased a library of 2,048 staple strands (that is, 32 positions × 32 handle sequences × 2 for complementary handles) that would allow any one of these handles to be encoded at any possible perpendicular slat intersection. In principle, subsets of staple strands could be selected from this library to create up to 32^{32} (~10^{48}) distinct 6HB (or $32^{16} \approx 10^{24}$ half-length 12HB using an analogous library strategy) slats (Fig. 1e).

We tested this library for growth of finite megastructures to determine the extent to which the strands could be rearranged to make novel shapes. The relative area, molecular mass and number of unique DNA origamis in each are shown in Fig. 1c. The smaller shapes with 48 and 64 slats have maximum lateral dimensions limited to 450 nm, the length of a 6HB slat (Supplementary Fig. 9a). To achieve larger dimensions, we also designed assembly trajectories where the 6HB slats join in a zigzagging raster-fill pattern where for a typical step, 16 parallel slats bind to each of two growth fronts that rotates 90° clockwise or counterclockwise (Supplementary Figs. 9b–d and 10). Using this raster-fill growth paradigm, we created larger megastructures including a 191-slat plus symbol, a 320-slat elongated plus symbol, a 568-slat heart, a ghost caricature with 954 slats and a sheet with 1,022 slats. The largest 1,022-slat sheet has lateral dimensions ~2 μm and a molecular mass of ~5.4 GDa, which is over an order of magnitude greater number of unique DNA origamis compared to fractal tiles than previously published[25] (Fig. 1c).

We selected strands from the handle library for independent folding of each slat. We then combined the folded slats into pools with maximally 100 unique members and concentrated each pool into a

https://doi.org/10.1038/s41565-022-01283-1

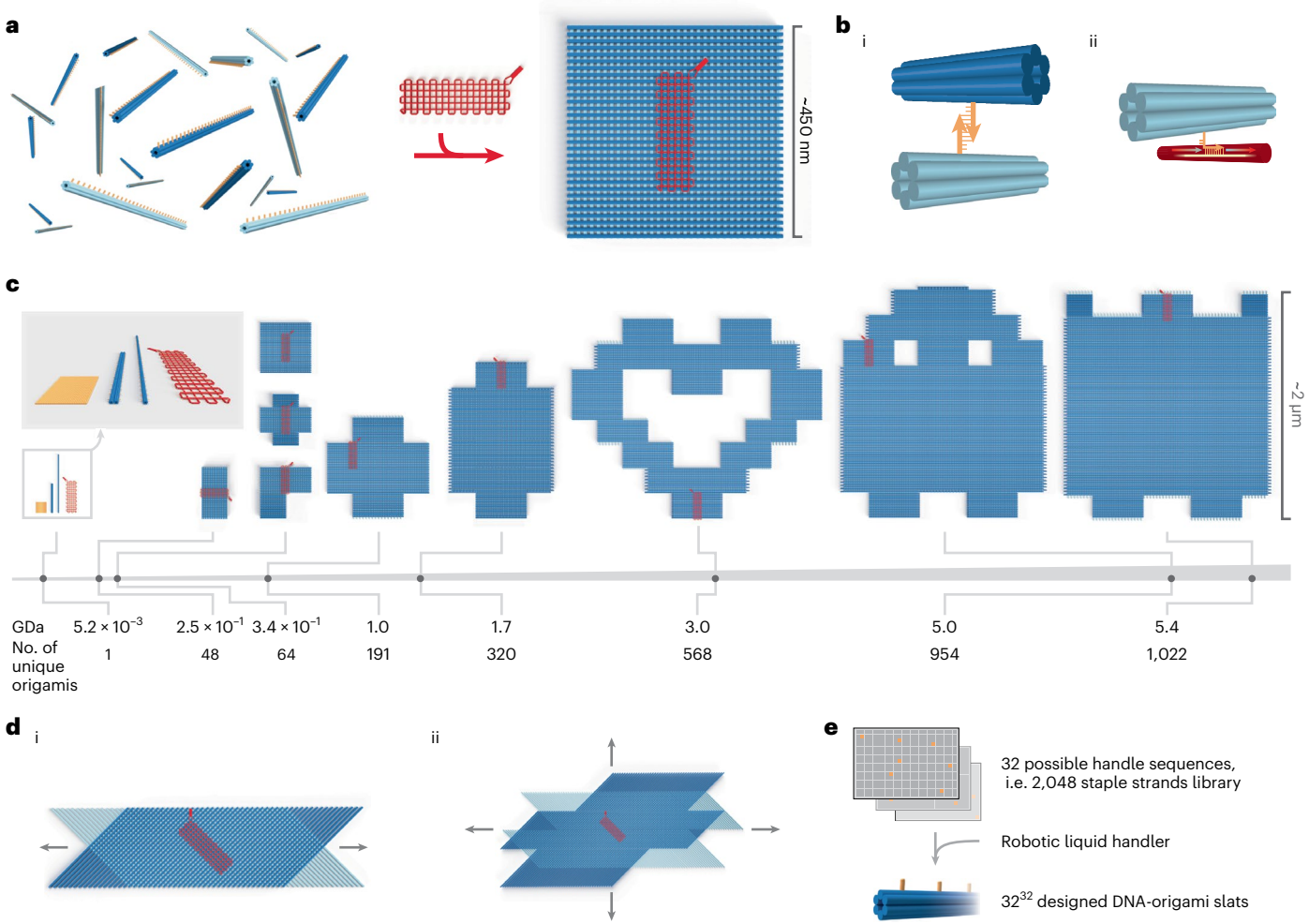

Fig. 1 | Overview of crisscross assembly of DNA-origami slats. a, Left: a pool of 64 unique free 6HB slats. A 6HB slat functionally comprises a linear arrangement of 32 binding-site sequences, each selected from the same set of 32 distinct sequences; right: a square megastructure with 64 unique slats is triggered to form only when the gridiron-origami seed is added. **b**, Binding of a pair of complementary weak 7 nt handles on two perpendicular 6HB slats (i); a strong 10 nt 'plug' handle on a 6HB slat engaged with an exposed region of scaffold (that is, a 'socket') on the gridiron seed (ii). **c**, The breadth and relative scale of the megastructures tested versus the leftward single DNA-origami slats, seed and origami reference square (85 nm × 85 nm). **d**, Renderings of periodic one-dimensionally (i) and two-dimensionally (ii) growing ribbons and sheets. **e**, Schematic for how subsets of the strand library are combinatorially collected to yield unique slats.

smaller volume (Supplementary Fig. 11). Crisscross growth was initiated by mixing a seed with top- and bottom-layer slat pools. The larger finite shapes with rastering growth (Supplementary Figs. 9c,d and 10, and Supplementary Video 1) were assembled in several stages, where ~200 of the slats were added and incubated for ~60 h before 2.5-fold dilution into a pool of the subsequent series of slats. We successfully assembled the panel of finite megastructures, as shown by TEM in Fig. 2. All the megastructures formed dispersed single particles in a seed-dependent fashion (Supplementary Figs. 12–15). The structures in Fig. 2a(i)–(v) were formed exclusively with 6HB slats, with the exception of the 1,022-slat sheet in Fig. 2a(vi) that also had 28 12HB slats. Half or more of the total slats in the Fig. 2b shapes were the shorter 12HB slats, allowing for the megastructures to have features finer than the length of a 6HB slat (Supplementary Text 2 and Supplementary Fig. 3).

To assess the relative incorporation of the 6HB slats into the megastructures, we counted the number of slats in higher-magnification TEM images in 64-slat squares. We determined an average incorporation of ~90% of the slats after overnight isothermal assembly, increasing to ~97% after an additional two days at room temperature (Fig. 2c(i),(ii)), which is comparable to the ~80–90% full incorporation of a given staple strand previously reported for some DNA origami structures[36]. We also assessed the relative completion of the largest finite megastructures by concentrating the final samples and looking to see if the features of each shape (that is, corners and middle sections of the shape were appropriately filled with slats) could be observed in lower-magnification TEM images. Greater than 22% of the megastructures for the 954-slat ghost and 1,022-slat sheet were fully grown as opposed to prematurely terminated (that is, all the major morphological features could be observed, as explained in Method 15) by the last assembly stage (N_{954_ghost} = 225, $N_{1,022\_sheet}$ = 267, see Supplementary Fig. 15). This suggests that over 75% of the assemblies at each stage were competent for continuing growth (that is, $0.78^n = 0.225$, where $n = 6$ growth stages. see caption of Supplementary Fig. 15).

Periodic ribbon and sheet megastructures

We used the strand library to create periodic 6HB-based crisscross ribbons and sheets (Fig. 3). We first explored the ribbons depicted in Fig. 3a, which grew bidirectionally from the first series of slats bound to the seed. In Supplementary Fig. 16a,b, each slat added is staggered one binding site unit compared to the parallel slat that preceded it,

https://doi.org/10.1038/s41565-022-01283-1

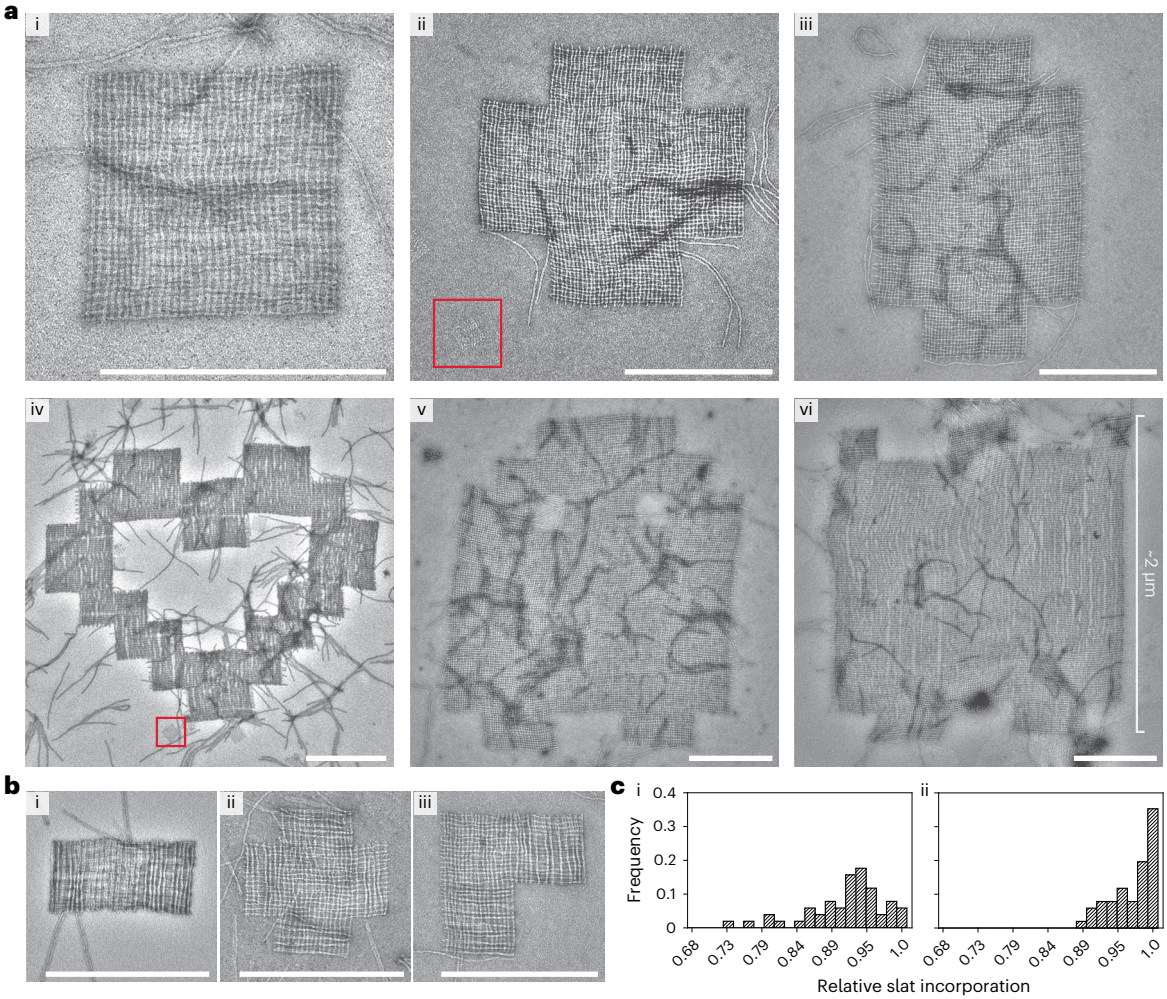

Fig. 2 | Assembly of finite megastructures from DNA-origami slats, where every slat is unique and addressable (see the designs in Fig. 1c). a, TEM images of megastructures composed entirely of 6HB slats, except for the 1,022-slat rectangle which has 28 horizontal 12HB slats in part (vi). The red boxed regions are a single origami reference square for size comparison, which is the largest area structure attainable with the same scaffold used for each slat. **b**, TEM images of finite megastructures where half or more of the slats are 12HBs. **c**, Histogram for the number of slats counted in close-up TEM images of 50 randomly selected finite squares. The squares were assembled at 34 °C overnight (i) versus assembled for an additional two days at room temperature (ii). Scale bars, 500 nm.

as similar to previously established for ssDNA slats[26]. The ribbons in Fig. 3a(i) versus Supplementary Fig. 17 are termed version 16 (v16) and version 8 (v8), respectively. In v16, a given slat has 32 perpendicular slats bound to all of its 32 possible binding handles, versus v8 which only has 16 slats bound to every other of its 32 possible binding sites. As observed by TEM, v16 ribbons appeared as relatively uniform flat ribbons as expected. In contrast, v8 ribbons were much more flexible and exhibited pronounced fluctuations in width along their lengths due to an accordion-style stretch. Furthermore, many v8 ribbons underwent full conversion to elongated spindles, although it is unclear from the images what the structure is (for example, whether this a simple accordion-style stretch taken to an extreme, or instead these are twisted as well) (Supplementary Fig. 18a,b). We also created ribbons with zigzag raster growth, where alternating clockwise then counterclockwise sets of 16 slat additions creates jagged edges, while alternating two clockwise sets with two counterclockwise sets creates flush edges (Fig. 3a(ii) versus Fig. 3a(iii); also see Supplementary Figs. 16c,d and 18c,d). Ribbons of all three design types attained comparable mean lengths after 16 h of isothermal incubation, despite the differences in programmed stagger (Supplementary Fig. 19).

For all periodic designs, the size of the repeating set of slats was explored from 8 to 64 unique slats in top and bottom layers each (Supplementary Fig. 20). However, most designs in this study were composed of 8 or 16 unique slats in the top and bottom layers each. We found that the apparent second-order rate constant for slat addition became progressively smaller as the overall slat concentration was increased to over 1–2 μM (Supplementary Text 4.1, and Supplementary Figs. 21 and 22). Consideration of this limiting behaviour motivated our strategy to grow our larger megastructures in multiple stages, sequentially adding subpools with only ~200 slats at a time to avoid lower than ~4 nM concentration of any one slat while maintaining total slat concentration close to 1 μM (Supplementary Text 4.2 and right-hand panels of Supplementary Figs. 9c,d and 10; the megastructure in Fig. 2a(iii) grew faster using the multistage protocol as shown in Supplementary Fig. 14).

We also created periodic 2D structures with the 6HB slats. One approach was to incorporate an additional layer of slats to a v8 ribbon to show that megastructures with more than two layers are possible (Fig. 3b and Supplementary Fig. 23). In this particular design, the bottom two layers of the v8 ribbon are locked into a rigid conformation

https://doi.org/10.1038/s41565-022-01283-1

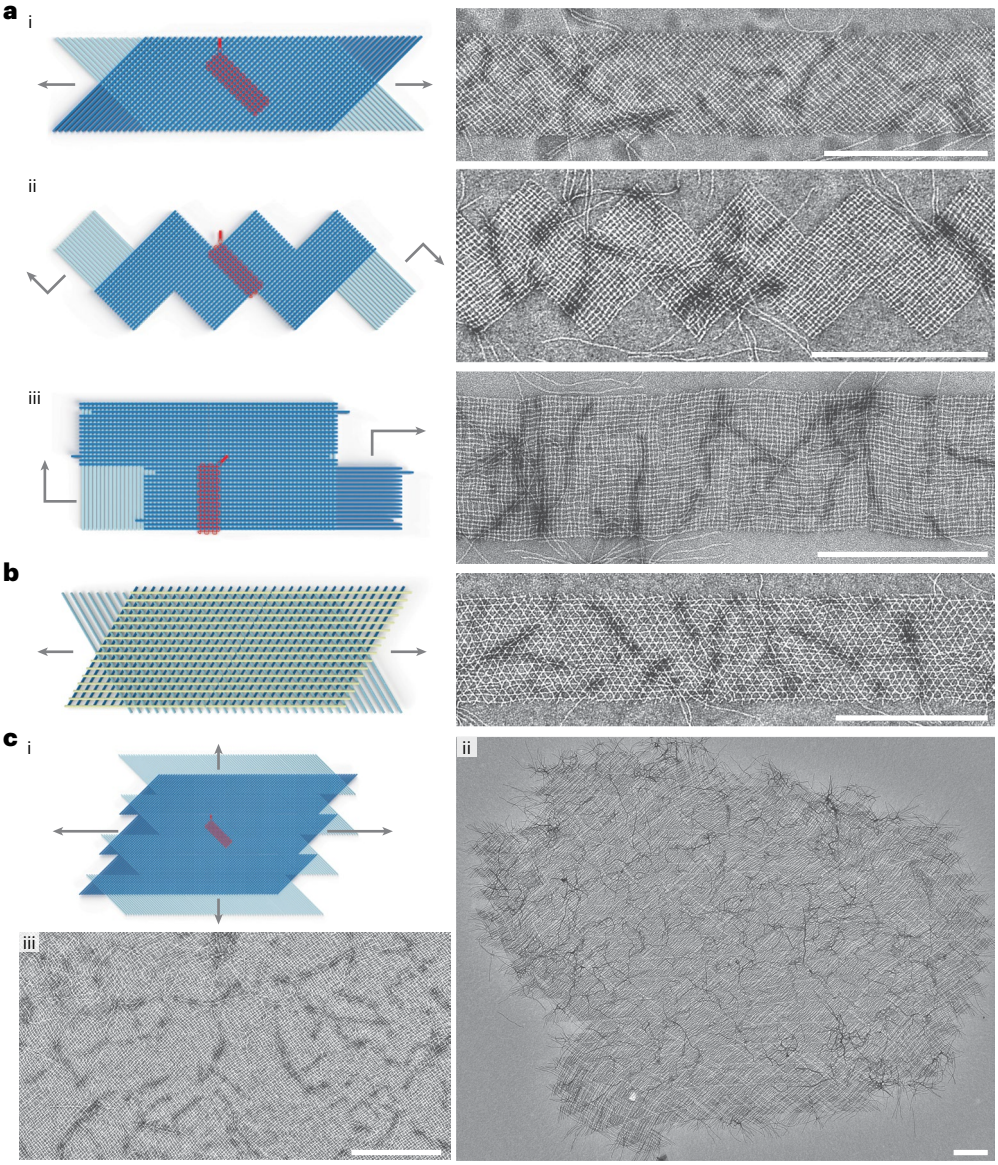

Fig. 3 | Assembly of periodic ribbons and sheets that grow with 6HB slats in one and two dimensions. a, v16 ribbon where top- and bottom-layer slats are staggered such that addition occurs in alternating order (i); v16 ribbon where the slats are added in a zigzag raster-fill pattern that creates jagged edges (ii); v16 ribbon where the slats are added in a zigzag raster-fill pattern that creates flush edges (iii). **b**, Trilayer arrangement of slats, where a top layer of yellow slats rigidifies the otherwise flexible v8 ribbon. **c**, Rendering of v16 growth from **a**(i) where slats are shifted to enable formation of a sheet that grows in two dimensions (i); TEM images showing an entire sheet positively stained with uranyl formate (ii), and a subset of another sheet with negative staining (iii). Scale bars, 500 nm.

where slats between layers are positioned 60° to one another. Next, we tested 2D sheets with two layers of slats (Fig. 3c). The design of the sheets is equivalent to the v16 staggered 1D ribbons shown in Fig. 3a(i), but with the bottom layer of slats shifted half of their lengths with respect to the top layer (Supplementary Fig. 24). These sheets, in this case defined by 16 + 16 slat unit cells with lateral dimensions of ~320 nm and containing 512 addressable nodes, typically grew to significant dimensions after three days of isothermal growth; the rightward example in Fig. 3c(ii) is composed of ~10,000 slats, with a molecular mass exceeding 50 GDa and lateral dimensions of ~10 μm (also see additional sheets in Supplementary Fig. 25). The higher-magnification TEM image in Fig. 3c(iii) shows a typical middle region of a sheet, with a fabric-like character where defects such as missing slats were infrequent. Both the 1D ribbons and 2D sheets were of sufficiently large molecular mass that they could be enriched over the excess unpolymerized slats by sedimentation into a pellet via centrifugation at 2,500 g (Supplementary Fig. 26 includes a discussion of the limitations of this centrifugation method, and a potential strategy for further enrichment). We also note that the ribbons were stable at room temperature for at least two days in $MgCl_2$ as low as 4 mM (Supplementary Fig. 27).

Addressability of megastructures

To illustrate that origami-crisscross megastructures can be functionalized as large addressable canvases, we designed the 1,022-slat sheet and periodic sheets to display custom patterns of handles on their top faces (Fig. 4a,b). We assembled a 10 nm DNA nanocube[37] contrast agent bearing a single complementary handle, incubated the patterned sheets with the purified nanocube and visualized the resulting patterns using negative-stain TEM (Supplementary Fig. 28). This incorporation

https://doi.org/10.1038/s41565-022-01283-1

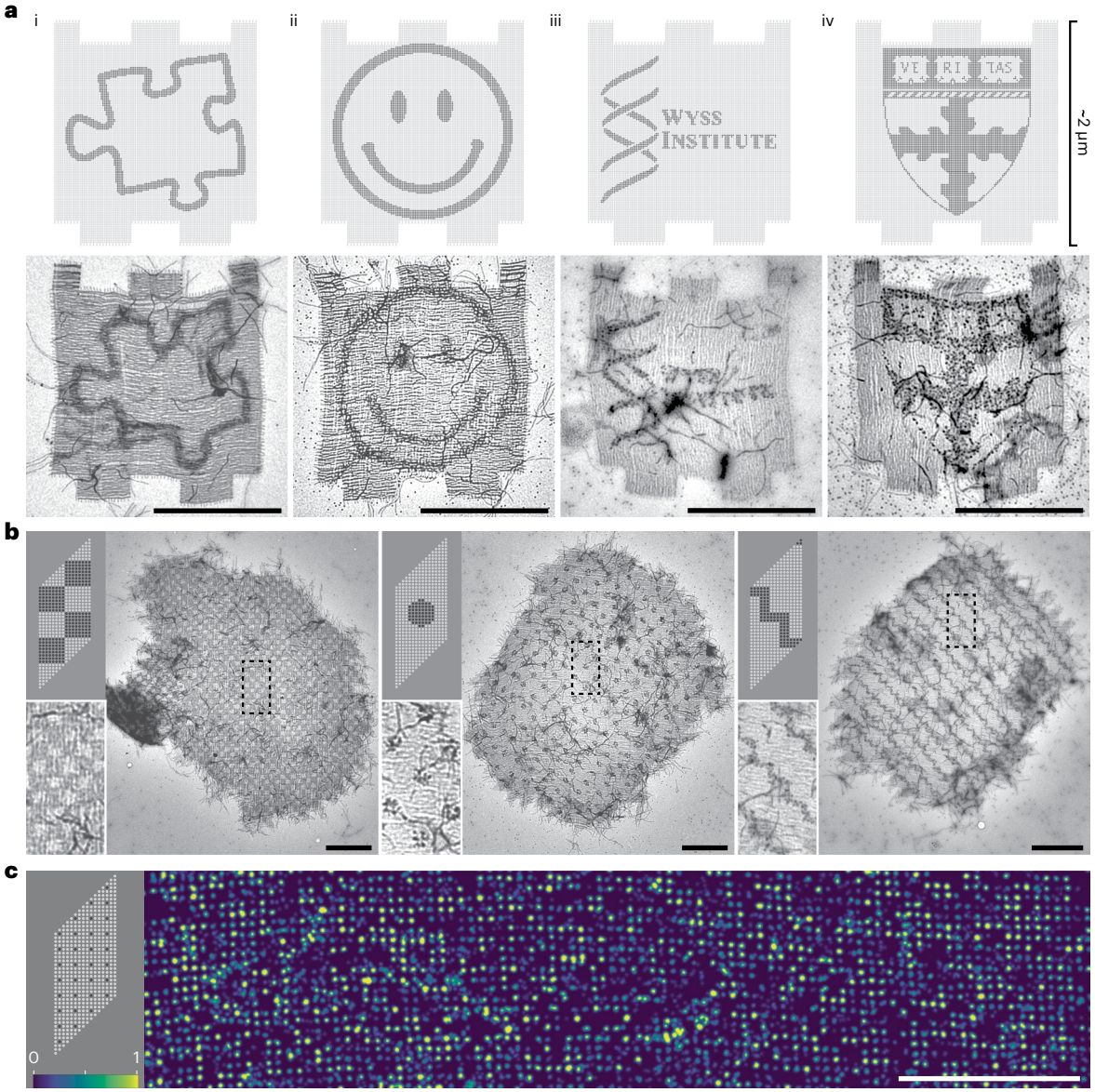

Fig. 4 | Finite and periodic crisscross megastructures as addressable DNA canvases to pattern arbitrary cargo. a, Top row: designs of the finite 1,022-slat sheet, with darker dots indicating sites that were programmed with a handle sequence to bind a DNA-nanocube contrast agent, with patterns including the outline of a jigsaw puzzle piece (i), a happy face (ii), and the crests for the Wyss Institute of Harvard University (iii) and the Harvard John A. Paulson School of Engineering and Applied Sciences (iv). Bottom row: TEM images of the patterned finite sheets. **b**, TEM images of 512-node periodic-sheet canvases patterned with DNA nanocubes, with the upper-left panels showing the designs. Boxed regions are shown more closely in the bottom-left panels. **c**, DNA-PAINT image of single handles on the sheets, as indicated in the top left design panel. Relative imager strand on-time is denoted by colour as shown bottom left. Scale bars, 1 μm.

could occur both during megastructure assembly or after via the incorporation of the complementary handles on the slats. The 1,022-slat sheets in Fig. 4a were observed to display the programmed patterning of intricate designs including a jigsaw puzzle piece, a happy face and institutional logos for some of our affiliations. Each ~2.0 μm × ~1.8 μm DNA canvas contains 16,128 addressable nodes, spaced ~14 nm apart. The nanocube was further used to decorate patterned 2D sheets, with the left panel of Fig. 4b showing the smaller 512-node canvas and the right panel showing a TEM overview of a chequerboard, a polka-dot sheet and a continuous jagged line. We additionally characterized the periodic 2D sheets and 1D ribbons using DNA-PAINT. We resolved single handles when spaced ~57 and ~43 nm (that is, 168 and 126 bp, respectively) between adjacent handles (Fig. 4c and Supplementary Figs. 29–31). Some lines of eight consecutive missing sites probably correspond to missing slats. In cases where washing steps are stringent enough to strip off slats to an appreciable extent, a future solution may be to crosslink handle interactions post-assembly. Other contiguous missing sites may be due to material lying on the megastructure, such as additional slats, that block access to probes.

Nucleation, kinetics and design rules

There was no observable formation of either finite or periodic megastructures in the absence of an added seed (Fig. 5a,b and Supplementary Fig. 32). We observed a linear one-for-one stochiometric dependence of megastructures formed to concentrations of seed added (Fig. 5c and Supplementary Figs. 33 and 34). To quantitatively assess spontaneous nucleation under various reaction conditions, we compared seeded v16 7 nt ribbons to unseeded control reactions with variations to temperature, concentration of slats or concentration of Mg^{2+} (Fig. 5d and Supplementary Figs. 35 and 36). We selected 34 °C as a reliable

https://doi.org/10.1038/s41565-022-01283-1

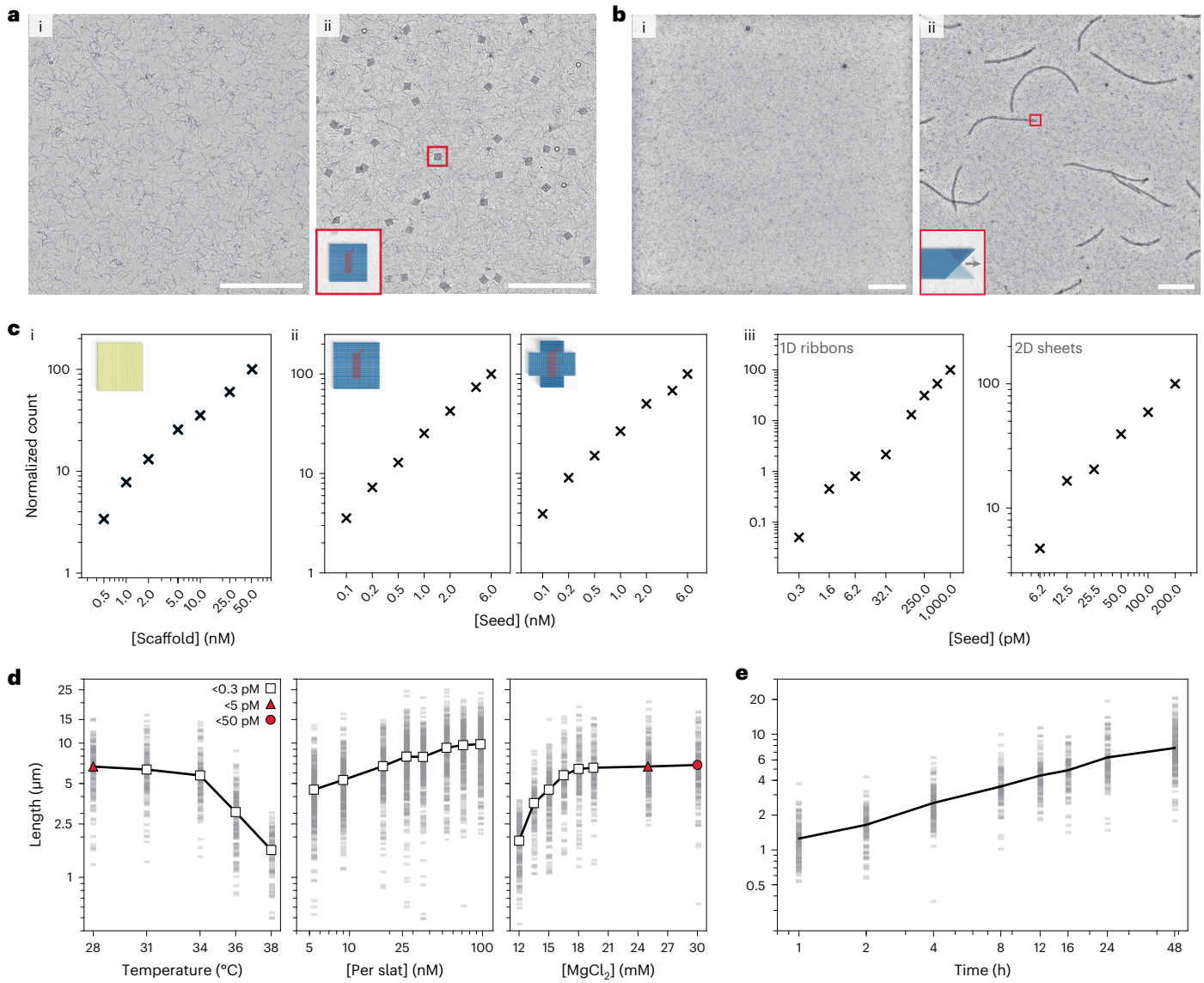

Fig. 5 | Characterization of growth versus reaction parameters. a,**b**, Seed-controlled assembly of the finite 64-slat square (**a**) and the periodic 1D ribbon (**b**) in low-magnification TEM images, with no seed versus seed in parts (i) and (ii), respectively. **c**, The number of DNA-origami squares formed versus the amount of scaffold added (i); the number of finite squares (left) or plus symbols (right) versus the amount of seed added (ii); and the number of periodic megastructures versus the amount of seed added (iii). The relative number of particles per condition is shown with the '×' marker. **d**, How the length of v16 1D ribbons with 7 nt binding sites varies as a function of temperature, concentration of slats and concentration of $MgCl_2$. Each faint grey bar is a single ribbon measurement. The white markers indicate no spontaneous assembly above the detection limit; red markers indicate where spontaneous assembly was observed to the degree shown in the legend in the leftmost plot. **e**, The length of the v16 1D ribbons versus time, grown at 20 nM of each slat. Axes in all plots are on a $\log_{10}$ scale, with the exception of the temperature and $MgCl_2$ scale in **d**. Particle counts in **c** were determined by counting structures in ten low-magnification TEM images, and ~150 ribbons were measured per condition in **d**,**e**. Scale bars, 5 μm.

temperature for robust and fast seed-controlled growth, without observable spontaneous nucleation (for further characterization of spontaneous nucleation of v8 and v16 ribbons, see Supplementary Text 5 and Supplementary Figs. 37–39).

The apparent second-order rate constant for slat addition, which we estimated at ~10^6 M^{-1} s^{-1}, was remarkably high (Supplementary Text 6, Fig. 5e and Supplementary Fig. 40). It is notable that these observed kinetics are comparable to those for hybridization of DNA strands[38], or up to two orders of magnitude faster than some other approaches to assemble DNA origami, such as blunt-end stacking of shape-complementary features (although these carry the advantage of stronger penalization of non-cognate interactions)[39]. Finally, we explored principles for combinatorial design of slats—using our 2,048 7 nt handle library—that are sufficiently orthogonal to support robust growth of complex megastructures (Supplementary Text 7 and Supplementary Figs. 41–45).

Conclusion

We generalized crisscross polymerization to DNA-origami slats for growth of diverse finite shapes including an addressable canvas from 1,022 unique slats that spans about 2 μm per side, periodic ribbons with several different extension patterns and periodic sheets that attained lateral dimensions exceeding 10 μm. Hierarchical self-assembly with these building blocks exhibited several features that are advantageous for rapid and robust nanoconstruction: (1) strict seed dependence of initiation, compatible with addition of slats at relatively high

concentrations and in stages; (2) relatively low defect rate in terms of missing slats and prematurely terminated megastructures, implying robustness in spite of inherent defects in the origami building blocks (for example, unavailable handles)[36]; (3) highly orthogonal behaviour that enables hundreds of distinct slats to assemble correctly in a single pot; (4) relatively large second-order rate constant for growth (10^6 M^{-1} s^{-1}) despite the 5 MDa size of the building blocks. Moreover, structural diversity was created by mixing and matching strands from a library of only 2,048 staple strands, where each binding handle of the slats was encoded with one of 32 possible sequences. Therefore prototyping diverse megastructures in this way is cost-effective.

In future studies, the design of the DNA-origami slats could be tailored to create a larger diversity of megastructure architectures[22], and various routes to more 3D structures—which would be more rigid than the two-layer structures predominantly investigated in this study—should be accessible[3,40–42]. As with other tiling approaches, it may be possible to programme growth with sophisticated algorithmic behaviours[43–45]. The resulting megastructures could provide access to templates for patterning of diverse guests, such as functional proteins and optically active nanoparticles, on length scales comparable to those of biological cells (Supplementary Text 8).

Online content

Any methods, additional references, Nature Portfolio reporting summaries, source data, extended data, supplementary information, acknowledgements, peer review information; details of author contributions and competing interests; and statements of data and code availability are available at https://doi.org/10.1038/s41565-022-01283-1.

References

1. Rothemund, P. W. K. Folding DNA to create nanoscale shapes and patterns. *Nature* **440**, 297–302 (2006).
2. Douglas, S. M. et al. Self-assembly of DNA into nanoscale three-dimensional shapes. *Nature* **459**, 414–418 (2009).
3. Andersen, E. S. et al. Self-assembly of a nanoscale DNA box with a controllable lid. *Nature* **459**, 73–76 (2009).
4. Benson, E. et al. DNA rendering of polyhedral meshes at the nanoscale. *Nature* **523**, 441–444 (2015).
5. Han, D. et al. DNA origami with complex curvatures in three-dimensional space. *Science* **332**, 342–346 (2011).
6. Han, D. et al. DNA gridiron nanostructures based on four-arm junctions. *Science* **339**, 1412–1415 (2013).
7. Marchi, A. N., Saaem, I., Vogen, B. N., Brown, S. & LaBean, T. H. Toward larger DNA origami. *Nano Lett.* **14**, 5740–5747 (2014).
8. Nickels, P. C. et al. DNA origami structures directly assembled from intact bacteriophages. *Small* **10**, 1765–1769 (2014).
9. Zhang, H. et al. Folding super-sized DNA origami with scaffold strands from long-range PCR. *Chem. Commun.* **48**, 6405–6407 (2012).
10. Wei, B., Dai, M. & Yin, P. Complex shapes self-assembled from single-stranded DNA tiles. *Nature* **485**, 623–626 (2012).
11. Ke, Y. et al. DNA brick crystals with prescribed depths. *Nat. Chem.* **6**, 994–1002 (2014).
12. Ong, L. L. et al. Programmable self-assembly of three-dimensional nanostructures from 10,000 unique components. *Nature* **552**, 72–77 (2017).
13. Ke, Y., Ong, L. L., Shih, W. M. & Yin, P. Three-dimensional structures self-assembled from DNA bricks. *Science* **338**, 1177–1183 (2012).
14. Pfeifer, W. & Saccà, B. From nano to macro through hierarchical self-assembly: the DNA paradigm. *ChemBioChem* **17**, 1063–1080 (2016).
15. Zhao, Z., Liu, Y. & Yan, H. Organizing DNA origami tiles into larger structures using preformed scaffold frames. *Nano Lett.* **11**, 2997–3002 (2011).
16. Wagenbauer, K. F., Sigl, C. & Dietz, H. Gigadalton-scale shape-programmable DNA assemblies. *Nature* **552**, 78–83 (2017).
17. Gerling, T., Wagenbauer, K. F., Neuner, A. M. & Dietz, H. Dynamic DNA devices and assemblies formed by shape-complementary, non-base pairing 3D components. *Science* **347**, 1446–1452 (2015).
18. Rajendran, A., Endo, M., Katsuda, Y., Hidaka, K. & Sugiyama, H. Programmed two-dimensional self-assembly of multiple DNA origami jigsaw pieces. *ACS Nano* **5**, 665–671 (2011).
19. Liu, W., Zhong, H., Wang, R. & Seeman, N. C. Crystalline two-dimensional DNA-origami arrays. *Angew. Chem. Int. Ed.* **50**, 264–267 (2011).
20. Woo, S. & Rothemund, P. W. K. Programmable molecular recognition based on the geometry of DNA nanostructures. *Nat. Chem.* **3**, 620–627 (2011).
21. Sigl, C. et al. Programmable icosahedral shell system for virus trapping. *Nat. Mater.* **20**, 1281–1289 (2021).
22. Yao, G. et al. Meta-DNA structures. *Nat. Chem.* **12**, 1067–1075 (2020).
23. Berengut, J. F. et al. Self-limiting polymerization of DNA origami subunits with strain accumulation. *ACS Nano* **14**, 17428–17441 (2020).
24. Wickham, S. F. et al. Complex multicomponent patterns rendered on a 3D DNA-barrel pegboard. *Nat. Commun.* **11**, 1–10 (2020).
25. Tikhomirov, G., Petersen, P. & Qian, L. Fractal assembly of micrometre-scale DNA origami arrays with arbitrary patterns. *Nature* **552**, 67–71 (2017).
26. Minev, D., Wintersinger, C. M., Ershova, A. & Shih, W. M. Robust nucleation control via crisscross polymerization of highly coordinated DNA slats. *Nat. Commun.* **12**, 1741 (2021).
27. Seeman, N. C. Nanomaterials based on DNA. *Annu. Rev. Biochem.* **79**, 65 (2010).
28. Kuzyk, A. et al. DNA-based self-assembly of chiral plasmonic nanostructures with tailored optical response. *Nature* **483**, 311–314 (2012).
29. Acuna, G. P. et al. Fluorescence enhancement at docking sites of DNA-directed self-assembled nanoantennas. *Science* **338**, 506–510 (2012).
30. Douglas, S. M., Bachelet, I. & Church, G. M. A logic-gated nanorobot for targeted transport of molecular payloads. *Science* **335**, 831–834 (2012).
31. Li, S. et al. A DNA nanorobot functions as a cancer therapeutic in response to a molecular trigger in vivo. *Nat. Biotechnol.* **36**, 258–264 (2018).
32. Shaw, A. et al. Binding to nanopatterned antigens is dominated by the spatial tolerance of antibodies. *Nat. Nanotechnol.* **14**, 184–190 (2019).
33. Derr, N. D. et al. Tug-of-war in motor protein ensembles revealed with a programmable DNA origami scaffold. *Science* **338**, 662–665 (2012).
34. Mathieu, F. et al. Six-helix bundles designed from DNA. *Nano Lett.* **5**, 661–665 (2005).
35. Douglas, S. M., Chou, J. J. & Shih, W. M. DNA-nanotube-induced alignment of membrane proteins for NMR structure determination. *In Proc. Natl. Acad. Sci. USA* **104**, 6644–6648 (2007).
36. Strauss, M. T., Schueder, F., Haas, D., Nickels, P. C. & Jungmann, R. Quantifying absolute addressability in DNA origami with molecular resolution. *Nat. Commun.* **9**, 1600 (2018).
37. Scheible, M. B. et al. A compact DNA cube with side length 10 nm. *Small* **11**, 5200–5205 (2015).
38. Zhang, D. Y. & Winfree, E. Control of DNA strand displacement kinetics using toehold exchange. *J. Am. Chem. Soc.* **131**, 17303–17314 (2009).
39. Bruetzel, L. K., Walker, P. U., Gerling, T., Dietz, H. & Lipfert, J. Time-resolved small-angle X-ray scattering reveals millisecond

transitions of a DNA origami switch. *Nano Lett.* **18**, 2672–2676 (2018).
40. Zhang, T. et al. 3D DNA origami crystals. *Adv. Mater.* **30**, 1800273 (2018).
41. Zheng, J. et al. From molecular to macroscopic via the rational design of a self-assembled 3D DNA crystal. *Nature* **461**, 74–77 (2009).
42. Tikhomirov, G., Petersen, P. & Qian, L. Triangular DNA origami tilings. *J. Am. Chem. Soc.* **140**, 17361–17364 (2018).
43. Rothemund, P. W. K., Papadakis, N. & Winfree, E. Algorithmic self-assembly of DNA Sierpinski triangles. *PLoS Biol.* **2**, e424 (2004).
44. Barish, R. D., Schulman, R., Rothemund, P. W. K. & Winfree, E. An information-bearing seed for nucleating algorithmic self-assembly. *Proc. Natl Acad. Sci. USA* **106**, 6054–6059 (2009).
45. Woods, D. et al. Diverse and robust molecular algorithms using reprogrammable DNA self-assembly. *Nature* **567**, 366–372 (2019).

Publisher's note Springer Nature remains neutral with regard to jurisdictional claims in published maps and institutional affiliations.

Springer Nature or its licensor (e.g. a society or other partner) holds exclusive rights to this article under a publishing agreement with the author(s) or other rightsholder(s); author self-archiving of the accepted manuscript version of this article is solely governed by the terms of such publishing agreement and applicable law.

© The Author(s), under exclusive licence to Springer Nature Limited 2022

Methods

Method 1: design and purchasing of handle staple strands

Binding sequences for the various handles were selected as explained in Supplementary Text 3. The handle sequences (and the complementary handle sequences) were appended to the 3′ end of either the top or bottom helix staple strands of the 6HB slat, where they were separated with a thymine (2T) linker. The binding handle sequences are reported in Supplementary Tables 6 and 7 (and also in Supplementary Data 1 as a spreadsheet), and the importance of the linker sequence is shown in Supplementary Fig. 8. All strands were purchased dry at full yield at the 10 nmol scale from Integrated DNA Technologies (IDT). We preferred to purchase the strands on Echo 525 compatible source plates (Labcyte #PP-0200) directly from IDT, although we sometimes ordered the strands on other plates and later transferred them to Echo 525 compatible source plates using a manual multichannel pipette. All strands were rehydrated in 50 µl of water, with their concentration assumed to be ~200 µM.

Method 2: design of sequence assignments (that is, permutations) of the handles from the library

See Supplementary Text 7 for an explanation of why care had to be taken in choosing permutations as described below, and Supplementary Data 2 and 3 for the final permutations. Blank layouts of top- and bottom-layer slats were drawn out in Microsoft Excel sheets after the megastructure design was initially conceived. Python scripts were then used to populate each cell of the blank Excel sheet randomly with a number ranging from 1 to 32, corresponding to a specific handle sequence from the 2,048-strand library. Next, the script converted the assigned sequences into a set of top-layer slats and bottom-layer slats, where each slat is defined as a 1D list that is 32 numbers long. The Hamming distances between the slats were measured to determine the number of handles on a given slat from one layer that matched together with complementary handles with each slat in the other layer. The process of random assignment and measurement of the Hamming distances in the resulting slats was repeated until some arbitrary maximum threshold of allowable kinetic-trap strength (that is, the minimum Hamming distance) was attained. We note that megastructure designs that were composed of larger numbers of unique slats tended to have more undesired matched complementarity compared to designs composed of smaller numbers of unique slats. One possible solution to further maximize the Hamming distances for a design would be to increase the size of the handle library (that is, using >32 different possible 7 nt handles at each slat intersection with a strand library that has >2,048 unique handle strands versus what was tested here). Nonetheless, we were able to attain satisfactory growth of megastructures that were composed with up to 1,022 unique DNA slats that were generated from the 2,048 7 nt handle library.

Method 3: pooling handle strands for each 6HB and 12HB slat and other folding details for preparation of slats on 96-well plates

Liquid handling protocols for each design were written to a csv file using Python scripts referencing the Excel sheet of the megastructure design (Method 2). Staple strands with or without handles were added into 96-well polymerase chain reaction (PCR) plates (Eppendorf E0030129512) from the 384-well strand library using a Labcyte Echo 525 acoustic liquid handler, which read the csv file using Echo Cherry Pick v.1.7.2. Each particular 6HB or 12HB slat, respectively, required transfer of 64 or 32 strands for the customizable top and bottom helices of the slat. We note that handle staple strands could also be pooled together manually using single-channel or multichannel pipettes, although such preparations could require an untenable amount of time depending on the number of slats in the megastructure. See Supplementary Fig. 11 for a time comparison of such approaches. After strand transfer into the 96-well plates, any droplets along the rim of the wells were spun down, at which point a slat-folding mixture containing other core strands, scaffold and buffer as specified in Method 4 was added to each well and mixed using a manual multichannel pipette. The 96-well plates were then thermally sealed with plastic films using an ABgene ALPS-300 microplate sealer and spun down one final time on a centrifuge, at which point plates were placed on a thermocycler and the origami folded using the temperature gradient in Method 4.

Method 4: design and folding of DNA origami

All DNA origamis were designed using legacy caDNAno[46] v.0. See Supplementary Data 5–8 for caDNAno json files of the 6HB, 12HB, gridiron seed, and single origami reference square. Staple and scaffold DNA sequences are reported in Supplementary Tables 1–5 (and also in Supplementary Data 1 as a spreadsheet). Unpurified dehydrated staple oligonucleotides were purchased from IDT at 100 or 10 nmol scale. For the slats, each unpurified core staple strand (that is, strands other than the 64 or 32 customizable handle strands for the top and bottom helices of the 6HB and 12HB slats, respectively) were rehydrated in water at ~1 mM and pooled together with equal volumes of each strand. For the gridiron seed and origami reference square, each dehydrated strand was resuspended in water at ~100 µM and pooled together with equal volumes of each strand. The p8064 and p8634 scaffold strands were produced from M13 phage replication in *Escherichia coli*. All folding was done in 1× TE buffer (5 mM Tris pH 8.0, 1 mM EDTA) with the $MgCl_2$ as specified below. The gridiron seed was mixed with 40 nM p8634 scaffold, ~250 nM of each staple strand, 10 mM $MgCl_2$, and folded with a 12 h temperature gradient: 94–86 °C in 5 min steps less 4 °C per step; 85–70 °C in 5 min steps less 1 °C per step; 70–40 °C in 15 min steps less 1 °C per step; 40–25 °C in 10 min steps less 1 °C per step; and 16 °C thereafter until the sample was collected. The 6HB slats were mixed with 50 nM p8064 scaffold, ~500 nM of each staple strand, 6 mM $MgCl_2$, and folded with an 18 h temperature gradient: 80 °C for 10 min as a single step; 60–45 °C in 160 6.75 min steps reducing by 0.1 °C per step; 16 °C thereafter until collection of the sample. The 12HB slats were mixed with 50 nM p8064 scaffold, ~500 nM of each staple strand, 8 mM $MgCl_2$, and folded with an 18 h temperature gradient: 80 °C for 10 min as a single step; 75–45 °C in 310 3.48 min steps less 0.1 °C per step; 16 °C thereafter until collection of the sample. The origami reference square was mixed with 40 nM p8064 scaffold, ~400 nM of each staple strand, 6 mM $MgCl_2$, and folded with an 18 h temperature gradient: 80 °C for 10 min as a single step; 60–45 °C in 160 6.75 min steps less 0.1 °C per step; 16 °C thereafter until collection of the sample. We note that there were special considerations for preparation of the slats in 96-well plates, as explained in Method 3.

Method 5: preparation of the DNA nanocube contrast agent

Unpurified dehydrated nanocube oligonucleotides were purchased from IDT at 10 nmol scale. Unpurified nanocube strands were rehydrated in water at ~100 µM each and pooled together with equal volumes per strand. Out of the 28 total nanocube strands as published previously[37], a single strand was selected and appended with a 4 T linker and 16 nt handle to its 3′ end (see sequences in Supplementary Table 8 or Supplementary Data 1). The nanocube was prepared with ~1 µM of each strand (with the handle-tagged strand at ~2 µM), 40 mM $MgCl_2$, and folded with a 42 h temperature gradient: 80 °C for 10 min as a single step; 65–37 °C in 290 8.69 min steps less 0.1 °C per step; 16 °C thereafter until collection of the sample. The folded nanocube was separated on an agarose gel and purified as described in Method 8, and bound to the megastructures without any further downstream assembly.

Method 6: agarose-gel electrophoresis

Gel characterization of the DNA-origami gridiron seed, 6HB slats or 12HB slats was performed using the Thermo Scientific Owl EasyCast B2 electrophoresis system. UltraPure agarose (Life Technologies, 16500500) was melted in 0.5× TBE (45 mM Tris, 45 mM boric acid,

0.78 mM EDTA, 11 mM $MgCl_2$) to a concentration of 1.0% (w/v). The molten agarose was cooled to 65 °C and 6.25×10^{-5}% (w/v) ethidium bromide was added. To assess folding, ~50 fmol of DNA-origami sample was mixed in an excess of agarose-gel loading buffer (5 mM Tris, 1 mM EDTA, 30% w/v glycerol, 0.025% w/v xylene cyanol, 10 mM $MgCl_2$; with typically 4 µl loading buffer added to 1 µl of each sample that was folded with 50 nM scaffold). The mixed samples were loaded onto the gel and separated for 3–4 h at 60 V at room temperature. Control samples for size and densitometry included one or both of the following: first, ~50 fmol of the same scaffold from which the DNA origami was folded; or second, ~0.5 µg of Gene Ruler 1 kb Plus DNA Ladder (Thermo Scientific SM1331). Gel images were captured on a GE Typhoon FLA 9500 fluorescent imager using the ethidium bromide parameters as given in the Typhoon control software. The photomultiplier tube was set to 500 V. Densitometry to quantify relative assembly of DNA bands was performed with FIJI ImageJ (v.1.53c)[47]. Background subtraction with a rolling ball radius of 30–60 pixels was performed on linear TIFF images. The GelAnalyzer plugin in ImageJ and the wand tool were used to integrate total pixel intensities from lanes of interest. DNA-origami yields were determined by taking the ratio of the intensity of the band of interest with respect to all the species with a molecular weight larger than the excess staple strands.

Method 7: PEG precipitation to concentrate pools of 6HB slats

The slats as folded on 96-well PCR plates were collected and combined into pools using a manual multichannel pipette. Each pool maximally had ~100 slats, although the number of slats in a given pool was variable depending on the design of the megastructure. We generally kept the slats in one layer of the megastructure in a separate pool from the perpendicular slats in the other layer of the megastructure, so that slats with complementary handles would not be concentrated in the same mixture together. Our rationale was that spontaneous interactions between the slats during concentration could be deleterious to the yield, although we did not study this carefully to determine whether such care was necessary. The pooled slats were subsequently concentrated using two rounds of PEG precipitation, as adapted from a published previously study[48]. The Mg^{2+} in the slat pool was increased from 6 mM to 20 mM by adding the appropriate volume of 1 M $MgCl_2$. One volume of 2× PEG-purification buffer (5 mM Tris, 1 mM EDTA, 15% w/v PEG-8000, 510 mM NaCl) was added and mixed with the equal volume of pooled slats in a 2 ml round-bottom tube. The mixture was spun at 16,000 g for 25 min, the supernatant was gently extracted using a pipette and the pellet was resuspended in 50 µl 1× TE buffer with 20 mM $MgCl_2$. The second round of PEG precipitation was performed using an equal volume of 2× PEG-purification buffer and the final slat pellet resuspended in a small volume of 1× TE buffer with 10 mM $MgCl_2$ so that the total concentration of slats was ~2 µM. However, the volume was adjusted as needed so that the pool was sufficiently concentrated to achieve the desired final per slat concentration in Method 9 or Method 10. The final slat pool was placed on a shaking incubator set to 1,000 r.p.m. at 33 °C for ~1 h. Finally, the concentration of DNA was measured on a Nanodrop 2000c spectrophotometer (Thermo Scientific) to estimate the final nanomolar concentration of slats.

Method 8: agarose-gel extraction to purify pools of 12HB slats

The 12HB slats in raw folded samples were low yielding and insufficient to prepare as described exactly in Method 7. See Supplementary Text 2, and Supplementary Figs. 3 and 4 where the yield and resulting challenges are discussed in detail. The 12HB slats were pooled as described in Method 7 and then separated on an agarose gel as described in Method 6. The gel was examined on an ultraviolet transilluminator to identify the monomer band, which was then excised from the gel using a razor blade. The gel-band pieces were transferred to a 1.5 ml Eppendorf tube, crushed using a plastic pestle and purified using Freeze N' Squeeze spin columns (Bio-Rad, 732-6166) as published previously[48]. The gel-purified samples were typically too dilute, such that it was necessary to concentrate them into a smaller volume of 1× TE buffer with 10 mM $MgCl_2$ using one round of PEG precipitation as explained in Method 7.

Method 9: preparation of megastructure assembly reactions with fewer than 200 unique slats

The raw gridiron seed (folded with 40 nM scaffold), purified slats (generally ~1 µM total slats per pool depending on the extent to which it was concentrated during purification) and 4× Megastructure buffer (5 mM Tris pH 8.0, 1 mM EDTA, 30 mM $MgCl_2$, 0.04% Tween-20) were mixed together in 5–20 µl at room temperature. We generally prepared the reactions in 0.1 ml Eppendorf PCR tubes (E0030124812) because of their tightly fitted lids which guarded against evaporative loss during extended growth periods. The final reaction generally contained ~0.5–2 nM seed, ~5–20 nM of each unique slat, 1× Megastructure buffer, with any excess volume filled with 1× TE buffer with 10 mM $MgCl_2$. We assumed that the seed and slats would be in 1× TE buffer with 10 mM $MgCl_2$, such that the final megastructure assembly reaction would contain 15 mM $MgCl_2$. Next, the reactions were placed on a thermocycler and incubated for 4 h at a high temperature where slats could only bind the seed (that is 45 °C or 55 °C for the 6/7 nt or 8 nt designs, respectively), before the temperature was lowered for slat growth for 1–72 h. We used 34 °C for typical growth of the v16 periodic and finite megastructures using the 7 nt handle library, versus other designs which used growth temperatures as summarized with cyan markers in the Supplementary Fig. 39 plot.

Method 10: preparation of megastructure assembly reactions with more than 200 unique slats

As explained in Supplementary Text 4, megastructures composed of a large number of unique slats (that is, >100 slats) generally grew slowly if all the slats were mixed simultaneously. Hence, designs with >100 unique slats were either incubated for a longer growth time, or grown in stages with several additions of slats. The first growth stage with ~200 of the slats most proximal to the seed were prepared as in Method 9. We prepared a 4× MultiMegastructure buffer (5 mM Tris pH 8.0, 1 mM EDTA, 22 mM $MgCl_2$, 0.024% Tween-20). In each stage thereafter, 5 parts of 4× MultiMegastructure buffer were added to 8 parts of an aliquot of the reaction from the previous stage with ~200 of the next slats in 20 parts total. The purpose of the 4× MultiMegastructure buffer was to maintain the buffer with 5 mM Tris pH 8.0, 1 mM EDTA, 15 mM $MgCl_2$, and 0.01% Tween-20 as more slats were added.

Method 11: binding of the DNA nanocube to 6HB-slat canvases

An aliquot of the sheet or 1,022-slat sheet was diluted 10- to 50-fold with agarose-gel purified nanocube solution from Method 5. The sample was incubated at room temperature overnight to bind the nanocube to the megastructures. The next day, the sample was purified from excess slats and nanocubes using two rounds of centrifugation, as outlined in Method 12. The sample was resuspended in 1× TE buffer with 10 mM $MgCl_2$ and 10% trehalose (w/v) and negatively stained with 1% uranyl formate, as described in Method 13. We qualitatively noted that trehalose and the lower percentage (that is, versus 2%) uranyl formate provided better contrast for the nanocubes on the megastructure canvas. The locations of nanocube handles on slats to create the desired patterns are shown in Supplementary Data 4.

Method 12: purification of periodic-ribbon and sheet megastructures by centrifugation

The largest periodic ribbons and sheets were purified from excess free monomers by centrifuging the samples at low speed. See Supplementary Fig. 26 for results using this method. Ribbons or sheets were prepared as in Method 9, diluted ~10-fold in 1× TE buffer with 10 mM $MgCl_2$, and then spun in a 1.5 ml Eppendorf tube at 2,500 g for 15 min.

The supernatant was gently extracted with a pipette and the pellet resuspended in 1× TE buffer with 10 mM $MgCl_2$ with the final volume as desired for the particular application. This procedure of centrifugation and resuspension could be repeated multiple times to further deplete excess free slats.

Method 13: TEM

Raw assembled megastructure reactions were diluted 1:250–1:1000 in 1× TE buffer with either 10 mM or 15 mM $MgCl_2$. TEM grids (Electron Microscopy Sciences; FCF400-CU, FCF200-CU-TA or FCF100-CU-TA) were negatively glow discharged at 15 mA for 25 s in a PELCO easiGlow. The diluted sample (4 µl) was applied to the glow-discharged grid, incubated for 2 min and wicked off gently into Whatman paper (Fisher Scientific, 09-874-16B). We used one of two possible approaches to stain the sample with 2% uranyl formate: (1) When closer-up structural detail of individual slats was desired, we used a negative-stain approach where 4 µl of 2% aqueous filtered uranyl formate was applied, incubated for 1–2 s, and gently wicked from its side into Whatman paper so as to leave a thicker deposit of uranyl formate around the sample. (2) When clarity of the overall forms and length of the megastructure was desired in low-magnification images, we used a positive-stain approach where 4 µl of 2% aqueous filtered uranyl formate was applied, incubated for 1–2 s and wicked off completely into Whatman paper to leave a thinner layer of uranyl formate, which darkened each particle with respect to the grid substrate. All imaging was performed at 80 kV on a JEOL JEM 1400 Plus microscope. All images presented in this work were imported into FIJI ImageJ (v.1.53c)[47], corrected for background noise using a pseudo flat-field image, and then contrast and brightness adjusted for clarity in publication.

Method 14: quantification of slat incorporation in TEM images

We used the finite 64-slat square as a model system to assess the relative incorporation of a given slat into a megastructure (see Fig. 2). Each sample was assembled for a given period of time, diluted 750-fold so that single squares could be differentiated from excess free slats on the TEM substrate, negatively stained with uranyl formate, and then imaged by TEM. Images of ~50 well-stained squares were collected at a magnification where the single slats could be differentiated. The slats in each layer of the square were quantified using the Cell Counter plugin in FIJI ImageJ (v.1.53c)[47].

Method 15: quantification of full growth of large finite megastructures in TEM images

Aliquots of megastructures with ~1,000 unique were concentrated ~10-fold and applied to TEM grids using a positive-stain approach (see Method 12 and Method 13, respectively). Sufficient numbers of low-magnification TEM images were collected so that ~200–300 individual megastructures could be assessed for their relative completion (that is, determining if the larger morphological features of the design—including edges and corners of the overall two-layer structure—were present with no observable missing segments). We alternatively considered doing Method 14 for the largest finite structures and periodic ribbons and sheets; however, the large number of slats in the megastructures, variable sizes of the periodic designs and manual approach to identifying the slats in images made this approach untenable. Thus sporadic missing slats were not considered in classifying megastructures as 'fully grown'. We view this as analogous to conventional analysis of DNA origami, where missing staple strands are hard to quantify and usually not considered as long as the overall structural integrity is intact.

Method 16: quantification of relative ribbon growth in TEM images

We used periodic ribbons to determine how parameters, including temperature, concentration of Mg^{2+}, concentration of the slats, time, strength of each binding site, the number of crisscross binding sites, growth pattern and sequence assignment influences growth (see Fig. 5d,e and Supplementary Figs. 19, 37, 38, 42 and 43). We assembled ribbons using 0.5 nM seed as explained in Method 9, diluted the initial sample 250-fold, and applied it to a grid where the structures were positively stained with uranyl formate. Each sample was then imaged at low magnification with TEM. We collected enough images so that at least 150 ribbons could be measured. The lengths of the ribbons were calculated using the NeuronJ plugin in FIJI ImageJ (v.1.53c)[47,49].

Method 17: quantification of stoichiometric control of megastructure formation from the seed in TEM images

We counted the number of megastructures in low-magnification TEM images of reactions where different concentrations of seed were added (see results in Fig. 5c). The raw samples were diluted to be able to see single particles in the condition where the highest amount of seed was added. We positively stained the sample with uranyl formate, and collected ten TEM images at a suitable magnification where the structure in question could be identified, but still allowed us to observe a reasonably large number of particles. The number of megastructures in each image was counted using the Cell Counter plugin in FIJI ImageJ (v.1.53c)[47]. We normalized the number of structures counted for a given seed concentration with respect to one of the concentrations tested and plotted the normalized count versus the concentration of seed (or scaffold) added.

Method 18: quantification of spontaneous nucleation of ribbons in TEM images

We counted the formation of periodic ribbons in control reactions with no seed to quantify the amount of spontaneous nucleation. We considered the ribbons useful as a model for spontaneous nucleation of megastructures because they were easy to identify as micrometre-sized objects that could be readily counted in low-magnification TEM images (see results in Fig. 5d and Supplementary Fig. 38). Samples were incubated at the reaction conditions that we desired to test, diluted ~250-fold, added to the TEM substrate, positively stained with uranyl formate, and then ten low-magnification TEM images were collected. The number of ribbons in each image was counted using the Cell Counter plugin in FIJI ImageJ (v.1.53c)[47]. The ribbons counted in each image area were normalized to the dilution and magnification, and then converted into a molar amount by comparing it to a standard curve of ribbons (Supplementary Fig. 35). The recorded ribbon detection limit was ~0.3 pM, which corresponded to observing a single ribbon in the ten images.

Method 19: preparation of megastructures for DNA-PAINT imaging

The outside faces of slats on ribbons and sheets were decorated on one side with 3′ complementary handle sequences for PAINT imager strands and on the other side with 5′ biotin sites. Slats were folded, purified, assembled into ribbons and sheets, and purified from excess slat monomers and resuspended in buffer B (5 mM Tris–HCl pH 8.0, 10 mM $MgCl_2$, 1 mM EDTA, 0.05% v/v Tween-20) at a final concentration of ~0.1 nM per megastructure as described in Method 4, Method 7, Method 9 and Method 12, respectively. The megastructure sample was further prepared as described previously[50], where an imaging chamber with an inner volume of ~20 µl was created by adhering one coverslip (#1.5, 18 × 18 mm^2, ~0.17 mm thick) to a glass slide (75 × 26 mm^2, 1 mm thick) with double-sided tape. Surfaces of the chamber were prepared by the following steps: (1) flowing 20 µl of 1 mg ml^{-1} biotin-labelled bovine albumin (Sigma-Aldrich, catalogue number A8549) dissolved in buffer A (10 mM Tris–HCl pH 8.0, 100 mM NaCl, 0.05% v/v Tween-20) and incubating it for 2 min; (2) washing with 40 µl of buffer A; (3) flowing 20 µl of 0.5 mg ml^{-1} streptavidin (Invitrogen, catalogue number S-888) dissolved in buffer A and incubating it for 2 min; (4) washing with 40 µl

of buffer A; (5) equilibrating with 40 µl of buffer B. Twenty microlitres of the purified biotin-labelled megastructure sample were then flowed into the chamber and incubated for 2 min followed by washing with 40 µl of buffer B. For the purpose of drift correction, fiducial markers (40 nm gold nanoparticles; Sigma-Aldrich, catalogue number 753637) were diluted to 1:10 in buffer B, flown into the chamber and incubated for 10 min followed by washing with 40 µl buffer B. Finally, imaging buffer (buffer B containing 2 U ml^{-1} protocatechuate 3,4-dioxygenase (OYC Americas, sold as rPCO), 2.5 mM protocatechuic acid (Sigma-Aldrich, catalogue number 37580), 1 mM Trolox (Sigma-Aldrich, catalogue number 238813)) was flowed into the chamber. The imaging chamber was sealed with nail polish before imaging.

Method 20: DNA-PAINT super-resolution imaging

DNA-PAINT imaging was performed on a Nikon Ti Eclipse inverted microscope with a Perfect Focus System and a custom-build TIRF illuminator. Laser excitation with a 532 nm laser (MPB Communications, 1 W, DPSS system) was used for excitation with a 100 mW input at an effective power density of ~2 kW cm^{-2}. The excitation laser was passed through a quarter-wave plate (Thorlabs, WPQ05M-532), placed at 45° to the polarization axis, and directed to the objective through an excitation filter (Chroma ZET532/10x) via a long-pass dichroic mirror (Chroma ZT532RDC_UF2). The laser beam was then expanded using a commercial variable beam expander (Edmund Optics, Broadband VIS 2X-8X) and a custom-built Galilean telescope followed by coupling into the microscope objective using a motorized mirror to generate a total internal reflection illumination. Emission light was spectrally filtered (Chroma ET542LP and Chroma ET550 LP), directed into a 4f adaptive optics system containing a deformable mirror (Imagine Optic, MicAO 3DSR) to correct optical aberration and optimize point spread functions, and imaged on a scientific complementary metal-oxide–semiconductor sCMOS camera (Andor Technologies, Zyla 4.2+) using rolling shutter readout at a bandwidth of 200 MHz at 16 bit and a 150 ms exposure time with 6.5 µm pixels, resulting in an effective pixel size of 65 nm. At each imaging session, 10,000 frames with an exposure time of 150 ms per frame were captured. DNA-PAINT image data were processed and rendered using Picasso[51]. The lateral positions of single-molecule localization events were determined using Picasso Localize followed by drift correction using imaged gold nanoparticles as fiducial markers.

Data availability

All raw TEM image data that were measured to determine growth and nucleation of origami crisscross megastructures are available upon request from W.M.S.

Code availability

Scripts that were used to make various assignments of handles of staple oligonucleotides, and scripts that were used to measure Hamming distances of sequence assignments, are available at https://github.com/aersh/origamicrisscross.

References

46. Douglas, S. M. et al. Rapid prototyping of 3D DNA-origami shapes with caDNAno. *Nucleic Acids Res* **37**, 5001–5006 (2009).
47. Schindelin, J. et al. FIJI: an open-source platform for biological-image analysis. *Nat. Methods* **9**, 676–682 (2012).
48. Wagenbauer, K. F. et al. How we make DNA origami. *ChemBioChem* **18**, 1873–1885 (2017).
49. Meijering, E. et al. Design and validation of a tool for neurite tracing and analysis in fluorescence microscopy images. *Cytometry A* **58**, 167–176 (2004).
50. Dai, M., Jungmann, R. & Yin, P. Optical imaging of individual biomolecules in densely packed clusters. *Nat. Nanotechnol.* **11**, 798–807 (2016).
51. Schnitzbauer, J., Strauss, M. T., Schlichthaerle, T., Schueder, F. & Jungmann, R. Super-resolution microscopy with DNA-PAINT. *Nat. Protoc.* **12**, 1198–1228 (2017).

Acknowledgements

We would like to thank the following individuals: J. Kishi for suggesting and helping write a grant for the Echo Acoustic Liquid Handler that made this work possible; S. Cabi and T. Zhang for helping test early designs of crisscross origamis; and V. Manoharan, M. Brenner, R. Sørensen and J. Hahn for the fruitful discussions. Funding was provided by a Wyss Core Faculty Award (W.S., P.Y.); a Wyss Molecular Robotics Initiative Award (W.S., P.Y.); National Science Foundation DMREF Award 1435964 (W.S.); National Science Foundation Award CCF-1317291 (W.S.); Office of Naval Research Award N00014-15-1-0073 (W.S.); Office of Naval Research Award N00014-18-1-2566 (W.S.); Office of Naval Research DURIP Award N00014-19-1-2345 (W.S.); NIH NIGMS Award 5R01GM131401 (W.S.); NSERC PGSD3-502356-2017 (C.M.W.); Alexander S. Onassis Scholarship for Hellenes (A.E.).

Author contributions

Conceptualization: C.M.W., D.M., A.E., J.F.B., W.M.S. Methodology: C.M.W., D.M., A.E., W.M.S. Software: C.M.W., D.M., A.E., G.G. Validation: C.M.W., D.M., A.E. Formal analysis: C.M.W., D.M., A.E., H.M.S., G.G. Investigation: C.M.W., D.M., A.E., H.M.S., G.G., J.F.B., F.E.C.D. Writing (original draft): C.M.W. Writing (review and editing): C.M.W., D.M., A.E., H.M.S., G.G., F.E.C.D., W.M.S. Visualization: C.M.W., D.M., A.E., H.M.S., J.F.B. Supervision: C.M.W., P.Y., W.M.S. Funding acquisition: C.M.W., D.M., A.E., P.Y., W.M.S.

Competing interests

A patent (PCT/US2017/045013) entitled 'Crisscross Cooperative Self-assembly' has been filed based on this work.

Additional information

Supplementary information The online version contains supplementary material available at https://doi.org/10.1038/s41565-022-01283-1.

Correspondence and requests for materials should be addressed to William M. Shih.

Reprints and permissions information is available at www.nature.com/reprints.